Modeling Firebrand Spotting in WRF-Fire for Coupled Fire-Weather Prediction

Maria Frediani[1], Kasra Shamsaei[1], Timothy W Juliano[1], Branko Kosovic[1], Jason Knievel[1], Sarah A Tessendorf[1], and Hamed Ebrahimian[1]

[1]Affiliation not available

March 15, 2024

Abstract

This study introduces the firebrand spotting parameterization implemented in WRF-Fire and applies it to the Marshall Fire, Colorado (2021) to demonstrate that, without fire spotting, wind-driven fire simulations cannot accurately represent the fire behavior. Spotting can be a dominant fire spread mechanism in wind-driven events, particularly those that occur in the wildland-urban interface (WUI), such as the Marshall Fire. To simulate these fires, the model's ability to spot is critical, in that it accelerates the rate of spread and enables the fire to spread over streams and urban features such as highways. The firebrand spotting parameterization was implemented in WRF-Fire to improve simulations of wind-driven fires in a fire-atmosphere coupled system. In the parameterization, particles are generated with a set of fixed firebrand properties, from locations vertically aligned with the fire front. Firebrands are transported using a Lagrangian framework and firebrand physics is represented by a burnout (combustion) parameterization. Fire spots may occur when firebrands land on unburned grid points. The parameterization components are illustrated through idealized simulations and its application is demonstrated through simulations of a devastating real case - the Marshall Fire (Colorado, 2021). The simulations were verified using time of arrival and contingency table metrics. Our metrics show that when fire spots were included in the simulations, fire rate of spread and burn area consistently improved.

1 Introduction

Firebrands or embers are burning pieces of materials (e.g., branches, bark, building materials) generated at a fire source and carried with the wind and convection. Fire spotting occurs when firebrands are lofted into the air, land on unburned areas, and ignite new fires (Fernandez-Pello, 2017). Spot fires are considered short-range within a few hundred meters from the source fire, or long-range, with reports of spotting distances as high as 35 km (Storey & others, 2021). Short-range spotting accelerates the fire rate of spread by expanding the fire perimeters beyond the fire front, whereas long distance spotting can ignite new fires several kilometers downwind, possibly in areas beyond containment boundaries. Fires driven by high wind speed combined with low relative humidity and flammable vegetation often result in high fire intensities, rapid growth rates, and showers of embers that can start new fires. Intense spotting increases danger to fire crews, affects fire behavior predictability, and challenges emergency response and containment efforts.

Embers play a significant role in spreading wildfires and are important especially in the wildland-urban interface (WUI; (Manzello et al., 2020)). When a fire reaches urban zones, it spreads through two primary mechanisms: (a) radiant and convective heat from adjacent structures; and (b) ember accumulation on flammable vegetation (e.g., lawns, mulch beds) or building components (e.g., leaf filled gutters, dry vents, porches, fences). In an urban setting, embers are the leading cause of home ignitions (Manzello et al., 2020).

When firebrands are not represented in fire behavior simulations, the predicted fire area can be considerably smaller than the observed. This is because the absence of spotting can underestimate the simulated fire rate of spread, while containment barriers depicted in the model fuels, such as streams and infrastructure, can prevent the simulated fire from spreading. (DeCastro et al., 2022) showed that some fire areas can be significantly different depending on the location of the ignition relative to nearby barriers. In the case of the 416 Fire (Colorado, U.S.), when ignition points were placed west of US 550, the fire area was significantly reduced because the fire spread towards the east was contained by the road.

Fire behavior simulations are intrinsically dependent on the model's fire fuels (Andrews, 2018; Ervilha et al., 2017). In addition to accurate depiction of burnable fuels (DeCastro et al., 2022), fuel barriers can also be misrepresented and affect simulation results. When it comes to fuel barriers (i.e., no fuel), accuracy is generally determined by the dataset spatial resolution combined with the spatial scale of containment features (water bodies, roads and other infrastructures). The continuity of fuel barriers depends on whether the dataset resolution can accurately represent the existing continuities. (Frediani et al., 2023) showed that when barriers appear as discontinuities in the fuels dataset, the simulated fire is able to spread. However, when barriers of large spatial scale, such as multiple-lane highways, are accurately depicted as continuous, the simulated fire cannot spread without a spotting capability.

The approach to modeling spotting depends on the fire behavior model to which it is combined. Fire behavior processes are frequently parameterized because resolving combustion and chemical processes is computationally expensive. The fidelity of the fire behavior and associated spotting parameterization (if present) also weighs on the computational costs and consequently determine their suitability for certain applications. FIRETEC (Linn et al., 2002) and WFDS (Mell et al., 2007) are examples of models using more comprehensive representations of fire behavior processes; however, their computational requirements make them unsuitable for operations. Consequently, the models used in fast-computation applications are simplified parameterizations mainly based on the Rothermel parameterization or cellular automata. These models include FARSITE (Finney, 1998), which is now incorporated into FlamMap (Finney, n.d.), Prometheus (Tymstra et al., 2010), BehavePlus (Andrews, 2014), and QUIC-Fire (Linn et al., 2020). These fire behavior models typically use atmospheric fields (winds, temperature, humidity) from numerical weather prediction models or wind simulators (Sanjuan et al., 2014), such that the fire responds to the atmosphere but the atmosphere does not respond to the fire (Mell et al., 2018).

Operational models typically used in fire management applications do not account for interactions between the fire and atmosphere, and their fire spread can be inconsistent with fire spreading characteristics (Ager et al., 2011). Conversely, models that couple atmosphere and fire (such as WRF-Fire, (Coen & others, 2013), WRF-SFire, (Mandel et al., 2014), FOREFIRE, (Filippi et al., 2010), and ARPS/DEVS-Fire, (Xue et al., 2012)) have the ability to resolve winds in complex terrain and model fire induced phenomena in the atmosphere (e.g., (Roberts et al., 2023)), which becomes more relevant with increasing fire scale and threat to communities adjacent to the WUI.

In the current literature, the effects of firebrand spotting in fire behavior simulations can be modeled with more computationally expensive computational fluid dynamics (CFD) models, such as the spotting implementation by (Koo et al., 2007) in FIRETEC and the coupled stochastic parametric model of firebrand transport by (Tohidi & Kaye, 2017), which provide high fidelity results comparable to wind-tunnel results. Yet, to be feasible for fire operation applications, firebrand spotting effects are vastly based on empirical models, typically based on spotting distance and probability of ignition ((McArthur, 1967; Tarifa, 1967; Tarifa et al., 1965; Albini, 1979; Albini, 1983; Ellis, 2015; Woycheese et al., 1998)), or incorporated into a cellular automata fire-spread framework (Alexandridis et al., 2011; Freire & DaCamara, 2019). Firebrands from urban structures specifically can be modeled by the implementations of (Himoto & Iwami, 2021) and the SWUIFT model by (Masoudvaziri et al., 2021).

The Firebrand Spotting parameterization described in this article was initially developed for the WRF-ARW model version starting at V4.4 (Frediani et al., 2023; Frediani et al., 2022; Frediani et al., 2022). The parameterization uses a Lagrangian particle transport framework to simulate firebrand advection, originating

in active fire points determined by WRF-Fire's fire behavior model, which is based on Rothermel's rate of spread model (Rothermel, 1972) coupled with a level-set algorithm to propagate surface fire (Munoz-Esparza et al. 2018).

WRF-Fire is an extension of the Numerical Weather Prediction (NWP) community model WRF-ARW and serves a distinct role amongst fire behavior models for its broadscale use in weather research and forecasting applications. Fires affect vertical convection and interfere with cloud formation and precipitation (Andreae et al., 2004; Bowman et al., 2009; Frediani & Rodriguez, 2008). Thus, fire simulation capabilities are an important component for simulating regional weather, and a mesoscale weather model without it is incomplete. With climate trends indicating fires are becoming larger and more frequent (McGinnis et al., 2023), fire and weather cannot be treated as independent phenomena in local and regional scales. The next generation of NWP models is being built based on the successes of the current ones. Hence, building upon the existing strengths, overcoming limitations, and understanding the forecast skill of current coupled models are critical pieces to the success of the upcoming generation of NWP modeling systems.

The firebrand spotting parameterization in WRF-Fire provides a more realistic representation of the fire physics, as it allows fire spots to accelerate the fire spread and initiate fires across barriers. Its overarching goal is to converge research relevant to fire-weather at local and regional scales by addressing an important fire behavior modeling limitation. This work is a novel step towards enhancing the numerical weather and fire prediction in WRF-Fire, and is a stepping stone to future advancements and potentially operational applications.

In this article, we use idealized simulations to describe the parameterization implementation, and demonstrate its application with a simulation experiment of the Marshall Fire. The article is divided into five sections: (1) Introduction; (2) Implementation of the Firebrand Spotting Parameterization, where we describe the parameterization components and associated methods; (3) Idealized Simulations, where we demonstrate the parameterization components through various idealized numerical experiments; (4) Marshall Fire Simulations, where we apply the parameterization to forecast the fire spread and quantify its accuracy; and (5) Conclusions.

2 Implementation of the Firebrand Spotting Parameterization

The Firebrand Spotting parameterization was developed for WRF-Fire in WRF-ARW versions starting at V4.4, with fire spot ignitions implemented in the upcoming V4.6.x. This subsection describes the most recent parameterization implementation. The source code is written in FORTRAN 2003 following the WRF model coding standards. It consists of two distinct modules, one containing the main firebrand spotting code and associated routines, and another, for specific Message Passing Interface (MPI) routines that were not part of the WRF model. Both modules are included within the WRF physics source code. The firebrand processes modeled by the parameterization are firebrand generation, transport, burnout, landing and ignition. In this Lagrangian framework, firebrands are modeled individually and may ignite fire spots at landing when ignition conditions are met. The main aspects of the parameterization are illustrated in Figure 1 and described in detail in the following subsections.

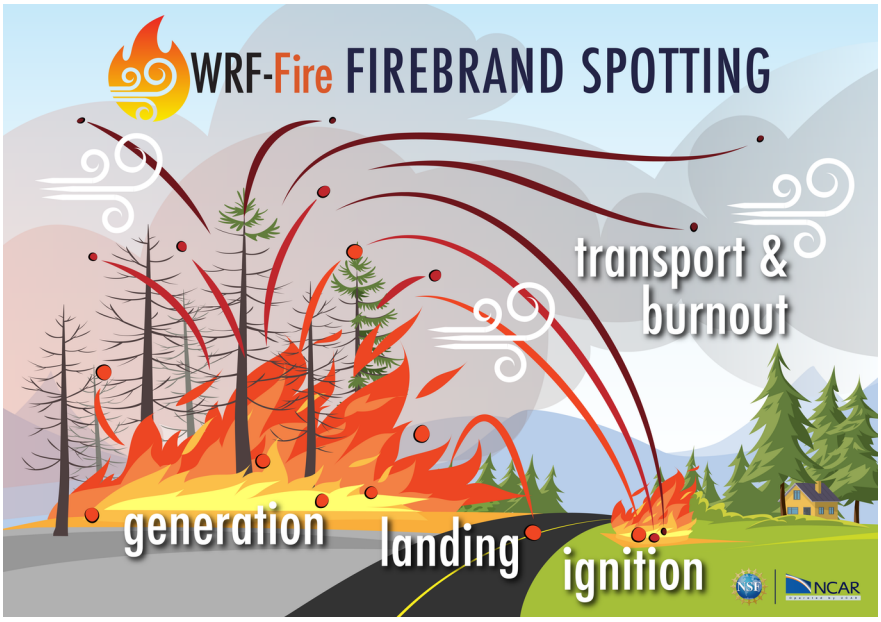

Figure 1: The firebrand processes modeled by the parameterization are firebrand generation, transport, burnout, and landing and ignition

2.1 Generation

The implementation of firebrand generation comprises a number of parameters that can be associated with distinct categories. I.e., generation locations are independently defined in the horizontal and vertical spaces, initial firebrand properties and momentum are configured by the user, and generation limit is associated with computational demand.

2.1.1 2-D Horizontal Generation (sources)

Firebrands are generated from grid points along the fire front where the fire rate-of-spread (ROS) is above a specified threshold (*fs_ROSthresh*). The frequency of generation cycles is defined by the generation period parameter (*fs_firebrand_gen_dt*) and generation sources comprise the 2-D grid points where the ROS threshold is met during the given timestep. Although indicated by (McArthur, 1967) and (Wadhwani et al., 2022) that firebrand generation is related to fire ROS, we do not prescribe a specific threshold. We include the generation period and ROS threshold parameters as user options to reduce the computational cost of transporting thousands of firebrands that could be generated at every timestep from every active fire grid point.

2.1.2 Vertical Generation

The number of vertical levels per source is set by the levels parameters (*fs_gen_levels*) and an associated maximum generation height (*fs_firebrand_gen_maxhgt*). Firebrands are evenly distributed between the maximum generation height and 1-meter above the landing height (*fs_firebrand_land_hgt*) by default, or can be randomly distributed between these levels if specified (*fs_firebrand_gen_levrand, fs_firebrand_gen_levrand_seed*).

2.1.3 Initial Firebrand Properties

Initial property parameters are set at time of generation and change during transport as the particles burnout. These parameters comprise diameter, effective diameter, temperature, and terminal velocity (fs_-

firebrand_gen_prop_diam, fs_firebrand_gen_prop_effd, fs_firebrand_gen_prop_temp, fs_firebrand_gen_prop_tvel), and are used during transport to parameterize burnout and terminal velocity. Currently, firebrand generation is limited to spherical particles with properties set by the user.

2.1.4 Initial Firebrand Momentum

A computationally inexpensive solution was implemented to account for firebrand initial momentum by accelerating particles downwind, which is the equivalent of allowing firebrands to travel without burning out or settling (*fs_firebrand_gen_mom3d_dt*) for a set number of timesteps. This option was implemented in lieu of effectively calculating an initial momentum to individual particles, which would require interpolation of atmospheric variables outside of the transport subroutines, and lead to further assumptions about the magnitude of firebrand momentum.

2.1.5 Generation Limit

The number of generation locations is defined by a source limit parameter (*fs_firebrand_gen_lim*), which is applied to the model's patch/tile when compiled for distributed memory parallel (dmpar) execution, or over the domain, when compiled for serial execution. This limit is meant to prevent overuse of memory and is patch/tile independent to decrease non-essential MPI communication.

2.2 Transport and Physics

After generation, the particles are transported in the three-dimensional space with the atmospheric flow, and burnout as advected. During transport, firebrands may burn out entirely or land, when trajectories descend below a given height threshold.

2.2.1 Advection

During transport, firebrands follow the resolved atmospheric flow as they burn out and fall. Particle density and char density (*fs_firebrand_dens, fs_firebrand_dens_char*) are the only user-defined parameters associated with firebrand physics. Firebrands may burn out entirely during transport, reach a maximum allowed lifetime (*fs_firebrand_max_life_dt*), or land.

During advection, the meteorological variables (wind, temperature, pressure, and air density) from the WRF model are interpolated from an Arakawa-C atmospheric (Skamarock et al., 2021) grid to each individual particle position using a bilinear method implemented following the particle trajectory model described in (Lee & Chen, 2014).

The source code for particle advection follows the approach implemented by the Hybrid Single Particle Lagrangian Integrated Trajectory (HYSPLIT) model (Stein et al., 2015), which uses an improved Euler method (also known as Heun's method, (Witty, 1964) to advect particles by the atmospheric wind. The method calculates the position after a full timestep by taking the average between the derivative (i.e., wind speed) at the starting position and the derivative at a full step forward:

$$\mathbf{x}_0^{t+1} = \mathbf{x}^t + \mathbf{U}_{\mathbf{x}}^t \Delta t$$

$$\mathbf{x}^{t+1} = \mathbf{x}^t + \frac{\Delta t}{2}(\mathbf{U}_{\mathbf{x}}^t + \mathbf{U}_{\mathbf{x}_0^{t+1}}^t)$$

where $\mathbf{x}_0^{t+1}$ corresponds to the position calculated at the first pass for a timestep forward $t+1$, $\mathbf{x}_{t+1}$ is the final advection position calculated at the second pass, $\mathbf{x}^t$ is the starting position at the starting timestep t, $U_{\mathbf{x}}^t$, and $U_{\mathbf{x}_0^{t+1}}^t$, are the wind speed at the starting position and first-pass position, respectively, and Δt is the timestep interval.

Particles are advected in the 3-D space using u, v, and w components of the wind, followed by an update of particle properties due burnout and fall speed.

2.2.2 Burnout

The parameterization for burnout is based on (Tse & Fernandez-Pello, 1998) and (Bhutia et al., 2010).

As the firebrand is transported by the ambient flow, its mass and volume (and consequently its diameter) decrease with increasing time due to pyrolysis, or the decomposition of material at high temperature. In the case here, woody material is pyrolyzed through both heterogeneous (glowing) combustion on the outer surface and homogeneous gas-phase oxidation of volatiles diffusing from within the firebrand (Albini, 1979). The pyrolysis front, which marches inward toward the particle center as woody material is converted into char, closely marks the region where heterogeneous combustion occurs. This demarcation is used to track what is referred to as the effective mass diameter, d_{eff}, as described in (Tse & Fernandez-Pello, 1998; Bhutia et al., 2010). It is implemented as

$$d_{eff} = \sqrt{(d_{eff}^{t-1})^2 - \beta \Delta t}$$

where the notation $t-1$ indicates the variable value in the previous timestep, β is a modified burning rate constant calculated as $\beta = \beta^0 \left(1 + 0.276 Re^{1/2} Sc^{1/3}\right)$, β^0 is an empirically-derived burning rate constant (β^0= 4.8E10^{-7}s^{-1}) from the data of (Tarifa et al., 1965), and Sc is the Schmidt number (assumed to be 0.7 for air; (Bhutia et al., 2010)).

As in (Tse & Fernandez-Pello, 1998), we calculate the Reynolds number R_e using the particle information

$$R_e = |W_r| \frac{d_p}{0.5 \left(\frac{\nu_{air}}{\rho_a} + \frac{\nu_p}{\rho_{ap}} \right)}$$

where $|W_r|$ is the relative velocity between the firebrand terminal velocity and the ambient vertical velocity, d_p is the particle diameter, ρ_{ap} is the air density surrounding the particle, ρ_a is the air density, ν_{air} and ν_p are the ambient kinematic viscosity and the kinematic viscosity immediately surrounding the firebrand, respectively. The kinematic viscosities are calculated as

$\nu = B \frac{T^{3/2}}{T+S}$, in which T represents the air or particle temperature, accordingly, B and S are the Sutherland's coefficients (B = 1.458 x 10^{-3} g msK^{-1} and S= 110.4K).

The firebrand particle mass is then calculated as

$$m_p = \frac{\rho_{wp} \pi d_{eff}^3}{6}$$

where ρ_{wp} is the particle's wood density (a used defined parameter with default value set to *fs_firebrand_dens* = 513,000 g m^{-3}). The particle volume V_p is given by $V_p = m_p / \rho_{wp}$. The updated diameter is given by

$$d_p^4 = (d_p^{t-1})^4 - \sqrt{3} \beta^2 \Delta t^2$$

In general, once a hot firebrand particle is generated and begins its traverse through the atmosphere, it cools due to convective and radiative heat losses. The temperature rate of change implementation for a spherical wooden particle is based on the influence of two heat transfer processes on the particle temperature using the energy equation:

$$\rho_{ap} V_p c_p \frac{dT_p}{dt} = -S_p(\mathbf{q}_{conv} + \mathbf{q}_{rad})$$

where V_p, c_p, T_p and S_p are the volume, specific heat capacity, temperature, and the surface area of the firebrand particle, and $\mathbf{q}_{conv}$ and $\mathbf{q}_{rad}$ are the convective and radiative heat fluxes, respectively, directed from the particle to the ambient air.

The net flux of heat transferred from a firebrand particle to the ambient flow due to convective processes is represented by

$$\mathbf{q}_{conv} = \overline{h}\,(T_p - T_a)$$

where T_a the ambient temperature near the particle and $\overline{h}$ is the average convection heat transfer coefficient, determined using the Nuselt number, $\overline{h} = \overline{Nu} k_{air}/d_p$, such that k_{air} is the air thermal conductivity (k_{air}=27). For a solid sphere, $\overline{Nu}$ may be calculated as

$$\overline{Nu} = 2 + 0.6 Re^{1/2} Pr^{1/3}$$

where Pr is the Prandtl number ($Pr = 0.7$).

The net flux of heat transferred from a firebrand particle to the ambient flow due to radiative processes is represented by

$$\mathbf{q}_{rad} = \sigma\epsilon\left(T_p^4 - T_a^4\right)$$

where σ is the Stefan-Boltzmann constant and ϵ is the emissivity of the firebrand.

We estimate c_p as the weighted average between wood and charcoal

$$c_p = \frac{d_{eff}}{d} c_{p_w} + \left(1 - \frac{d_{eff}}{d} c_{p_c}\right)$$

were c_{p_w} is the specific heat capacity for wood ($c_{p_w} = 1466$ J kgK^{-1}) and c_{p_c} for charcoal ($c_{p_c} = 712$ J kgK^{-1}).

Lastly, the time rate of change of firebrand temperature is then implemented as

$$\Delta T_p = -\frac{6}{\rho_{ap} V_p c_p d_p}\left(\overline{h}(T_p - T_a) + \sigma\epsilon(T_p^4 - T_a^4)\right)\Delta t$$

2.2.3 Fall Velocity

It is assumed the particle fall speed is equal to its terminal settling velocity, which for a spherical particle may be written as

$$V_t = \sqrt{\frac{\rho_{ap} d_p g}{3\rho_a C_D}}$$

where g is gravitational acceleration, and C_D is the drag coefficient. As in previous studies (e.g., (Tse & Fernandez-Pello, 1998; Bhutia et al., 2010)), we assume $C_D = 0.45$. Our assumption that firebrand fall speed is immediately equal to V_t is reasonable considering that typically reach their terminal velocity within seconds.

2.3 Landing and ignition

Firebrands land when their vertical position reaches a defined height threshold (*fs_firebrand_land_hgt*) over an unignited grid point. A spotfire is ignited when the number of firebrands landing on a given grid point, where fuel load is greater than 0 Kg m^{-3}, meets two specified criteria. The ignition criteria are defined to allow ignitions when (a) firebrands land on a grid point and adjacent neighbors, comprising up to 8 adjacent grid points, reflecting a spatial likelihood (Eq. 14), and (b) a specified number of firebrands land on a grid point and adjacent neighbors, reflecting an intensity likelihood (Eq. 15). The criteria are made of two independent thresholds: 1) the number of neighboring grid points (*fs_ignneighb*) and 2) the total number of firebrands landing on the grid point and adjacent neighbors (*fs_ignthresh*).

$$N = \sum_{i-1}^{i+1} \sum_{j-1}^{j+1} 1, \text{ if } (f_{ij} > 0) \text{ AND } (fuelload_{ij} > 0)$$

$$T = \sum_{i-1}^{i+1} \sum_{j-1}^{j+1} f_{ij}, \text{ if } (fuelload_{ij} > 0)$$

where i and j are the grid point indices, N represents the number of neighbors, T is the threshold for the total number of landing firebrands, f_{ij} represents the number of landed firebrands on the corresponding grid point during the current timestep, and *fuelload* is the fuel load on the corresponding grid point during the current timestep.

The set value for *fs_ignneighb* can be as low as 1, referring to the central grid point *ij* itself, and as high as 9, referring to the central grid point and the 8 adjacent neighbors. When both *fs_ignneighb* and *fs_ignthresh* are set to zero, ignitions do not occur.

At this stage of development, the firebrand parameterization in WRF-Fire is a framework that enables firebrand simulation and consequently more adequate fire propagation in WRF-Fire. The framework allows for future contributions, such as those described by (Manzello et al., 2020) and (Wadhwani et al., 2022), including for example implementation of a more sophisticated generation process, advection and burnout of non-spherical particles, and empirical ignition criteria, which would certainly improve the model capability. This article is intended to validate the framework and serve as reference for continuing developments in future version releases.

3 Idealized Simulations

In this section we illustrate the parameterization components through a set of idealized simulations using WRF-ARW v4.5.1 for two idealized scenarios:

3.1 Uncoupled

The first scenario is an "uncoupled" scenario in which the feedback from the fire to the atmosphere (i.e., the release of fire heat fluxes to the atmosphere) is turned off, and the surface boundary condition is set to be free-slip. In this configuration, the atmospheric conditions, including the wind speed and direction, remain constant during the simulation. This scenario is configured to eliminate environmental factors that can affect the firebrands generation and transport in order to validate the implemented parametrization. For this scenario, the atmosphere's horizontal grid interval is set to 40 m, with refined fire grid interval of 5 m. The model top is set at 2 km with 51 equally spaced grids. The timestep of the simulation is set to 0.5 s with open lateral boundary conditions. The simulations are initialized with a surface temperature of 305K and an air temperature vertical profile constant in the lower 1 km (300 K) below a statically stable

layer in the upper 1 km, with temperature increasing linearly to 310 K at the top. The fuel in the fire grid is homogeneous and set to Anderson's 13 fuel category 10, which corresponds to timber litter with understory, and the fire is ignited using a 1 km long and 100 m wide ignition line 10 s after the simulation start time.

3.2 Coupled

The second idealized cases scenario is configured in large-eddy simulation (LES) with two-way feedback, in that the fire fluxes are transferred to the atmosphere allowing for turbulent eddies and a fire-induced atmospheric circulation. In this scenario, the atmosphere's grid interval is set to 10 m and the refined fire grid interval to 5 m. The model top is set at 2 km with 51 vertically stretched grids. The timestep of the simulation is reduced to 0.125 s to account for the finer grid mesh and fire updrafts. The lateral boundary condition is periodic and the Deardorff's turbulent kinetic energy subgrid-scale model is utilized with coefficient of 0.1. The simulations in this scenario are initialized using the same temperature profile employed in the uncoupled scenario. We impose an initial zonal wind speed of 10 m s^{-1} (unless otherwise specified), interacting with an idealized surface with heat flux of 100 W m^2 and drag coefficient of 0.005. To facilitate the turbulence development in the model, a temperature perturbation bubble with magnitude of 0.5 K and depth of 40 m was utilized. The simulations were allowed to "spin-up" for 0.5 h prior to fire ignition in order to develop the turbulent boundary layer. After the spin-up, the fire is ignited using a 1 km long and 40 m wide ignition line on a homogenous fuel bed set to Anderson's fuel type 10.

In both of these scenarios, fire spots remained off to reduce degrees of freedom and allow a proper assessment of the parameterization components. Unless otherwise specified, the parameterization settings used in these simulations were set to the values indicated in Table 1, column Ideal Scenarios.

Table 1: Firebrand spotting parameterization settings and default values

Firebrand Process	**Parameter Category**	**Namelist Parameter**	**Default Value**	**Ideal Scenarios**
-	Maximum Array Size	fs_array_maxsize	100,000	100,000
Generation	Gen. Limit	fs_firebrand_gen_lim	0 (off)	0 (off)
Generation	Horiz. Gen. Threshold	fs_ROSthresh	0.1 m/s	0.1 m/s
Generation	Horiz. Gen. Period	fs_firebrand_gen_dt	5 timesteps	5 timesteps
Generation	Vertical Gen.	fs_firebrand_gen_levels	5	3
Generation	Vertical Gen.	fs_firebrand_gen_maxhgt	50 m	35 m
Generation	Vertical Gen.	fs_firebrand_land_hgt	0.15 m	0.15 m
Generation	Vertical Gen. Random	fs_firebrand_gen_levrand	false	false
Generation	Vertical Gen. Random	fs_firebrand_gen_levrand_seed	1	1
Generation	Gen. Momentum	fs_firebrand_gen_mom3d_dt	0	0
Generation	Initial Properties	fs_firebrand_gen_prop_diam	10 mm	3.6 mm
Generation	Initial Properties	fs_firebrand_gen_prop_effd	10 mm	3.6 mm
Generation	Initial Properties	fs_firebrand_gen_prop_temp	900 K	900 K
Generation	Initial Properties	fs_firebrand_gen_prop_tvel	0 m/s	0 m/s
Transport and Physics	Constant Properties	fs_firebrand_dens	513,000 g/m^3	513,000 g/m^3
Transport and Physics	Constant Properties	fs_firebrand_dens_char	299,000 g/m^3	299,000 g/m^3
Transport and Physics	Advection	fs_firebrand_max_life_dt	200 timesteps	200 timesteps
Landing and Ignition	Landing	fs_firebrand_land_hgt	0.15 m	0.15 m
Landing and Ignition	Ignition	fs_ignneighb	0	0
Landing and Ignition	Ignition	fs_ignthresh	0	0

3.3 Idealized Analysis

Firebrand generation is primarily dependent on the fire ROS. The fire ROS and corresponding number of generated firebrands 40 min after ignition is shown in Figure 2. The figures show a sequence of generation cycles for the uncoupled (panel A) and couple (panel B) cases, occurring between 2-minute outputs given the respective model timesteps and generation cycle periods. On the left side, the figure shows the fire ROS at the latest timestep, and on the right side, the number of generated firebrands accumulated between outputs. The fire ROS advances with wind direction whereas the accumulation of generated firebrands is denser over areas where (1) ROS is above the default threshold of 0.1 m/s, and (2) ROS is slower, because more firebrands were generated from the same grid point during the accumulation interval. In the uncoupled simulation, ROS is symmetrical and winds are uniform. In the coupled simulation, the wind speed and direction are influenced by the fire heat flux, which in turn drives an asymmetrical ROS, leading to a heterogeneous firebrand generation.

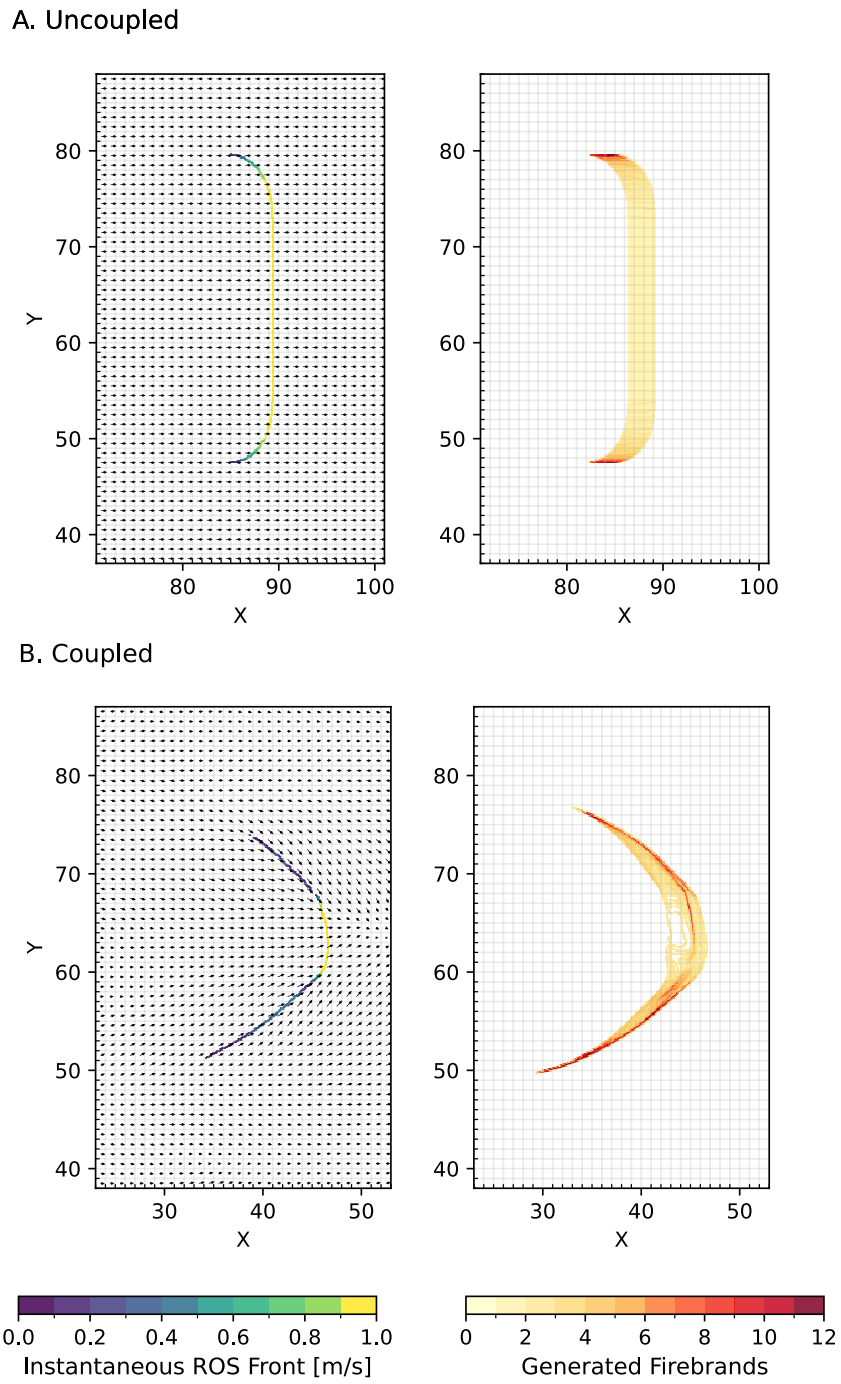

Figure 2: Fire ROS and number of firebrands generated during one of the model's history intervals for (A) uncoupled and (B) coupled simulations.

We illustrate transport through firebrand travel distances and trajectories from a set of simulations configured with various wind speed and particle properties (diameter, temperature, and density). In Figures 3 and 4, the parameters for the sensitivity tests are chosen to be representative of real-world scenarios. More specifically,

firebrand density and diameter are chosen to result in typical firebrand mass of 0.01 g to 1 g based on the available data in the literature (Filkov et al., 2017; Tohidi et al., 2015). Due to unavailable data for firebrand temperature, we selected a range based on reasonable values for smoldering and flaming combustion. The wind speed upper range is limited by the small simulation domain, in that in higher wind speeds, the fire reaches the domain boundaries, forcing the termination of the simulation.

The travel distance sensitivities due to particle properties and wind speed is shown in Figure 3. Each parameter is tested with three different values, using both coupled and uncoupled configurations. In the uncoupled scenarios, travel distances among firebrands generated at the same heights do not vary within each simulation because firebrands are generated with fixed-value properties, the atmosphere profile is homogeneous, and the wind vector is constant. In the coupled scenarios, travel distances vary due to turbulence, which develop as the fire heat perturbs the wind field. Firebrands will travel farther if generated where the local flow is upward and forward.

In the uncoupled simulations, the travel distances are illustrated by the dashed vertical lines. These simulations show that for the same wind speed (10 m s^{-1}) and for the range of parameters simulated, cooler and smaller, firebrands burn out faster. On average, the median travel distance increases by 1.44 m for each 100 K warmer, and by 3.8 m for each mm larger. The effect of particle density (spherical particles in this case) is more subtle - the median distance decreases by 0.015 for each kg m^{-3} denser. Although subtle, the overall sensitivity to particle density indicates that a higher number of lower density particles travel longer distances. Lastly and as expected, wind speed is a primary factor affecting firebrands' reach - the median travel distance increases by 3.3m for each m s^{-1} increase.

Because firebrand generation is a function of fire ROS, which in turn is a function of wind speed, the number of firebrands generated increases as we increase the background wind speed. In the simulations for the coupled scenario, 828, 844, and 1832 firebrands were generated for 5, 10, and 15 m s^{-1} wind speed, respectively, whereas in the uncoupled scenario simulations, the number of firebrands was 598, 624, and 652 firebrands.

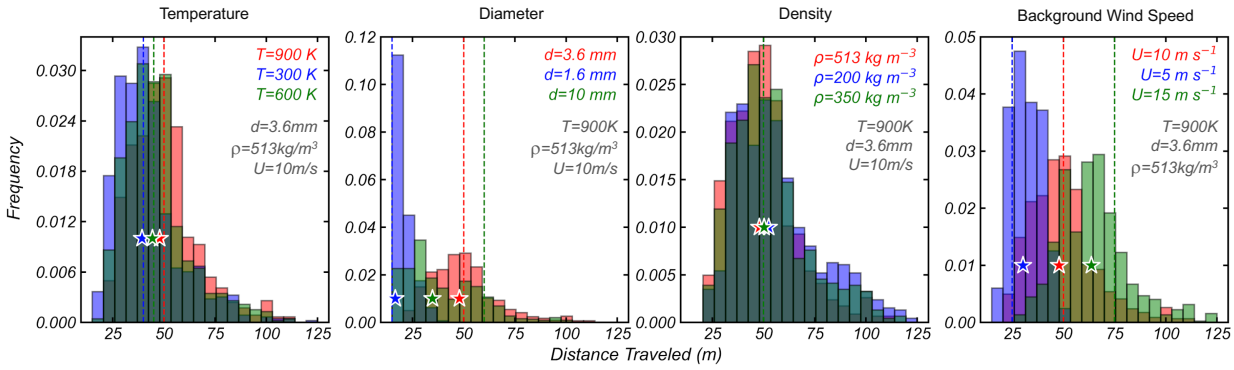

Figure 3: Travel distance sensitivities for different firebrand temperatures, diameters, densities, and background wind speed. The varying parameters (T, d, ρ, and U) are displayed on the corresponding plots in red, blue, and green, and the fixed parameters are indicated in gray. At the bottom of each plot, the star indicates the distribution medians for the coupled simulations. The distances for the uncoupled simulations are indicated by the vertical dashed lines.

Figure 4 shows a subset of randomly selected particle trajectories in a vertical cross-section, recorded for a 2-min interval starting 30 min after ignition. In the uncoupled cases, the trajectories of particles with the same properties are parallel because the wind speed is constant and thus they travel the same distances. Whether

they land or burnout depends only on their initial properties and height from where they are released, not on the environment. In the coupled cases, the trajectories depend on the particle's interaction with the local wind. In these simulations, 2055 particles were tracked, from which 225 landed and 1830 burned out.

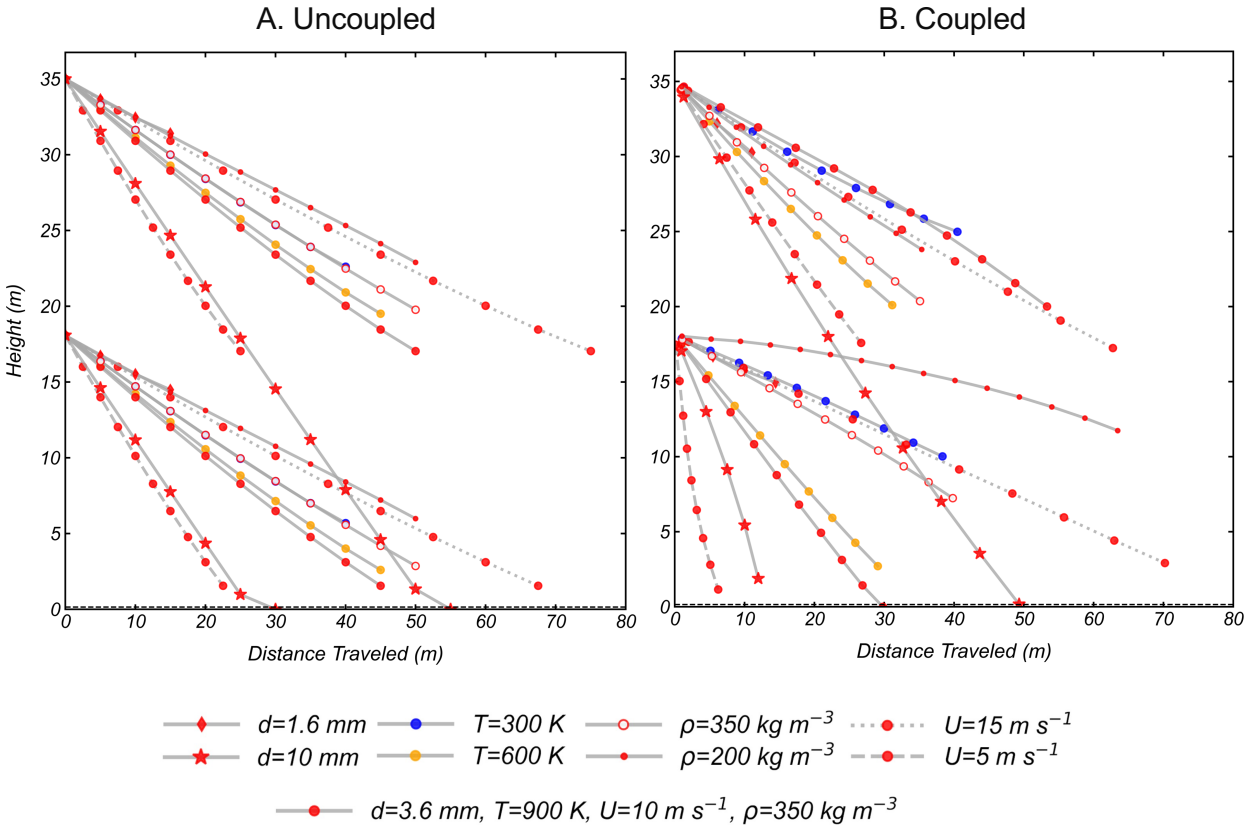

Figure 4: Vertical cross-section showing particle trajectories for a subset of firebrands from (A) uncoupled and (B) coupled simulations.

Figure 5 shows the effect of different ignition criteria on the associated number of fire spots, resulting fire area, fire ROS, and firebrand generation. The ignition criteria is configured with total thresholds and number of neighbors of 1 and 3, such that t indicates the total threshold and n the number of neighbors (i.e., t1n1, t3n1, t1n3). The black lines (dashed and solid) show the uncoupled and coupled simulations without fire spots, i.e., firebrands are generated and transported but do not ignite fire spots.

When fire spotting is enabled, a higher number of fire spots (panel A) occurs in the simulations with the lowest thresholds (t1n1, blue lines) and their the fire area increases faster (panel B), as expected. However, due to the rapid fire propagation in t1n1, the number of generating sources (i.e., points where fire ROS is above the specified threshold, panel C) is lower than t1n3 and t3n1 (green and yellow lines), which is also reflected in the number of firebrands generated (panel D).

When fire spots are not present, the fire ROS (panel C) increases almost linearly with time. In the absence of turbulence (uncoupled), the number of generated firebrands (panel D) also increases linearly with time, whereas when turbulence is present, the firebrand generation varies approximately with the number of generating sources. This variation is approximate because the generation interval is longer than the model

timestep (*fs_firebrand_gen_dt* = 5); hence the local maxima of generating sources may not always coincide with a generation cycle.

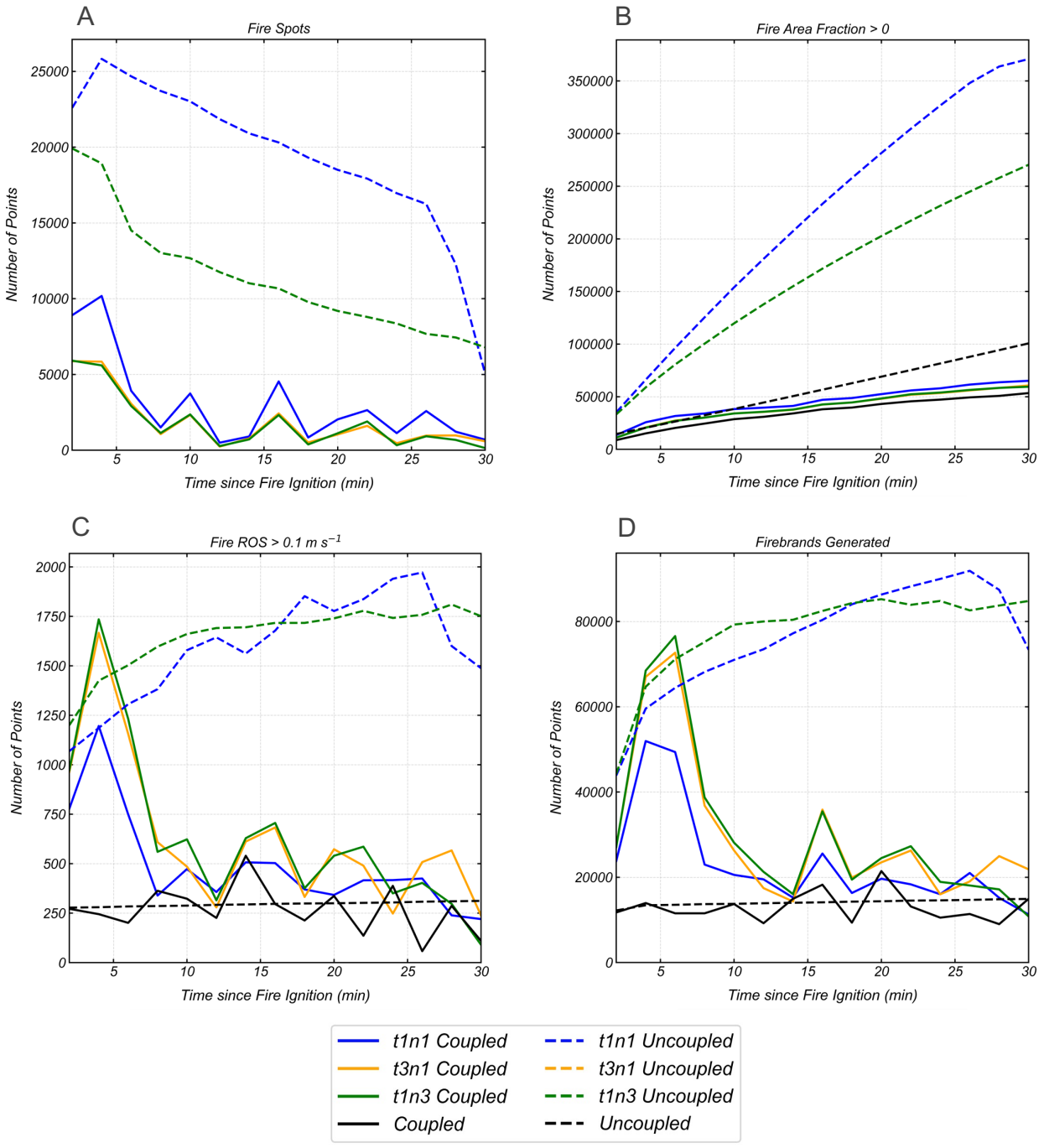

Figure 5: Effect of ignition criteria on (A) number of fire spots, (B) fire area, (C) fire ROS, and (D) firebrand generation. The ignition total threshold is indicated by t and number of neighbors indicated by n. The black lines (dashed and solid) show the uncoupled and coupled simulations without fire spot ignitions.

4 Marshall Fire Simulations

The Marshall Fire started in the outskirts of Boulder, Colorado on 2021/12/30 approximately at 18Z (11 AM MT) and reached the residential area in about 1 hour. To this date, the Marshall Fire is the most destructive in Colorado's State history, with 1084 homes destroyed and 149 damaged. According to the Boulder County Operational After-Action Report (OAAR, (County, 2022)), the fire initiated from two distinct sources, a downed utility line and a shed on fire in the same area.

That particular year had an unusually wet and warm spring season, which allowed grasses to grow taller and thicker; but from June to December, the area experienced the warmest and driest year on record, leading to favorable fuel conditions (Dougherty & Johnson, 2023). The fast spread was driven by a downslope windstorm, with wind gusts records of 100 mph, relative humidity around 20%, and cured grass fuel. The event was described by (Fovell et al., 2022) as "a perfect storm of fast winds and drought conditions as the combination of historically warm temperatures and low precipitation along the Front Range of the Rocky Mountains left the grasses in a state of extreme dryness".

This analysis of the Marshall Fire simulations concludes the preliminary work by (Frediani et al., 2022), where we encoded four spotting ignitions in WRF-Fire, representing strategic fire spot locations that allowed the fire to spread across roads and Hwy36. Our preliminary work enabled (Juliano et al., 2023) to simulate and analyze the physical drivers of its spread and evaluate the simulated atmospheric flow characteristics using Doppler on Wheels (DOW) observations.

4.1 Simulation Configuration

The Marshall Fire was simulated on Derecho HPC (Computational and Information Systems Laboratory, CISL, 2023) using WPS v4.5, WRF v4.5.1, and a developmental version of the firebrand spotting parameterization. The simulations were configured with two nested domains (parent and child, Figure 6), with one-way feedback between domains, at horizontal grid intervals of 1000 and 111m, using a mesoscale to microscale configuration (e.g., (Haupt et al., 2019)) in which the inner nest runs in LES mode. We used a fixed 3-s time step, 45 vertical levels, fire grid refinement of 4, and boundary conditions from the High-Resolution Rapid Refresh (HRRR) model (Dowell et al., 2022; Blaylock, 2019) at 3-hourly intervals. The physics processes were modeled with the following parameterizations: WRF Single-Moment 6-class scheme as the microphysics (Hong & Lim, 2006), RRTMG (Iacono et al., 2008) and Dudhia scheme (Dudhia, 1989) for long and shortwave radiation, Yonsei University scheme (Hong et al., 2006) for Planetary Boundary Layer (in parent domain only), revised MM5 for surface layer (Jiménez et al., 2012), and Noah Land Surface Model (Ek et al., 2003).

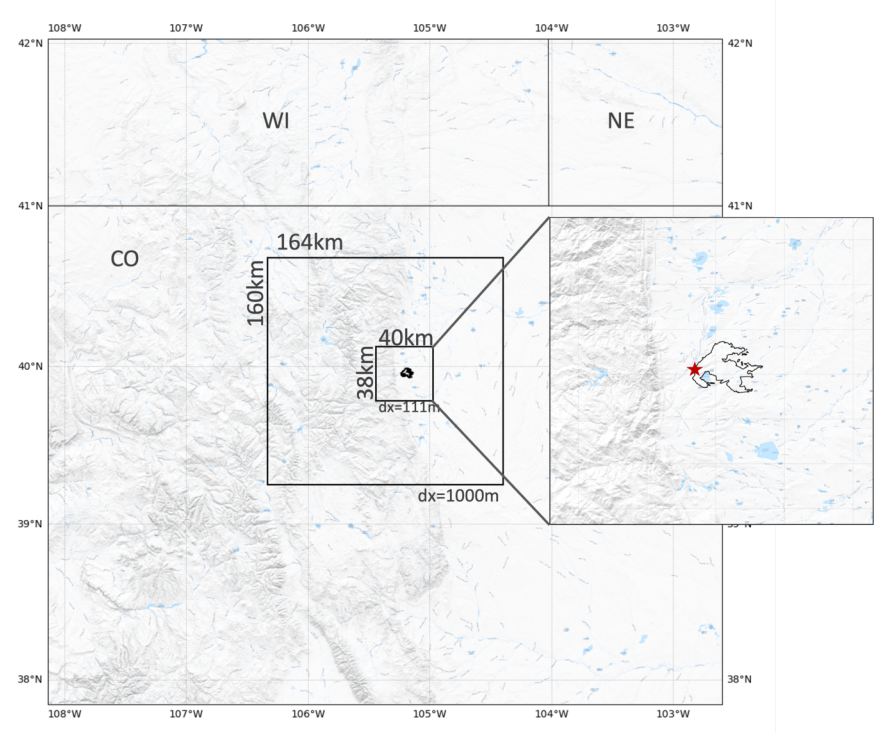

Figure 6: Simulation parent and child domains, Marshall Fire observed perimeter (black outline) and ignition location (red star)

For the fire behavior, we used fuels from the Anderson 13 fuel models obtained from the LANDFIRE database ("13 Anderson Fire Behavior Fuel Models (LF 1.4.0)", n.d.), and a 100-m ignition line at (start: -105.230189, 39.956029) and (end: -105.230784, 39.956225), representing the approximate location considered during police investigations, ignited 5 minutes after model initialization. The firebrand spotting parameterization was configured with firebrands generated at every other timestep (*fs_firebrand_gen_dt* = 2), 10 evenly distributed vertical levels (*fs_firebrand_gen_levels* = 10), firebrand momentum of 6 timesteps (*fs_firebrand_gen_mom3d_dt* = 6), and 3-m land height corresponding to the approximate height in meters of the infrastructure in the area (*fs_firebrand_land_hgt* = 3).

The ignition sensitivity experiments were configured with various combinations of *fs_ignthresh* and *fs_ignneighb* , such that t indicates the value used for *fs_ignthresh* (t for total) and n indicates the value for *fs_ignneighb* (n for neighbor) (Table 2). Hereafter we refer to these experiments as "txny Fire-Spots" experiments.

Table 2: Fire-Spots experiments

Name	**Total Threshold**	**Number of Neighbors**
t5n1	5	1
t5n2	5	2
t5n3	5	3
t3n3	3	3
t10n1	10	1
t10n2	10	2
t10n3	10	3
t15n3	15	3

Name	Total Threshold	Number of Neighbors
t3n5	3	5
t5n5	5	5
t10n5	10	5
t6n6	6	6

4.2 Forecast Verification Methods

In atmospheric sciences, forecast verification refers to the process of assessing the quality of forecasts through methods involving comparisons between forecasts and observations (Wilks, 2011; Jolliffe & Stephenson, 2012; Murphy & Winkler, 1987; Murphy, 1996). In this subsection, we describe the observations and methods used to quantify the accuracy of the forecasted fire behavior.

Ember showers were mentioned in multiple news sources, including on the OAAR, and also appeared in multiple social media videos; however, firebrands were not directly measured or estimated. Considering that embers were a primary fire spread mechanism in this fire, we verify the simulated fire spread instead. The fire spread is verified against the observed fire perimeter and point observations compiled from recorded footage.

The official containment fire perimeter was time stamped four days later, once the fire was 100% contained. However, according to the OAAR, most of the fire spread occurred during the daytime in the ignition day: "at approximately 6:30 PM, the wind decreased to 25-30 mph and the fire behavior decreased in intensity and rate of spread." The report indicates that at 8 PM MT "weather conditions had notably changed from the prior 9 hours", and although crews continued to fight fires through the night, we have not found records that indicated significant fire spread overnight. With that in mind, we consider the official fire perimeter was not substantially different from a perimeter that would have been produced on the night of December 30th.

In addition to the fire perimeter, the simulated fire spread is assessed using timestamps from recorded footage, compiled by a special project by 9News in Denver (KUSA-TV) (("Burned The Story Behind the Marshall Fire", n.d.)), combined with records from the operational response in the OAAR. We used footage that enabled us to define approximate timestamps at fixed and explicitly identifiable locations within the footage. The timestamps and locations are summarized in Table 3.

To align the observations with the model output, we reassigned the reported time to the closest model output and moved the location coordinates to the nearest point where fuel load was greater than zero, still inside the fire perimeter. The locations had to be slightly moved because the Anderson fuels used by the model had a considerable number of points categorized as urban fuels (corresponding to a category with no fuel load), which would result in the model being unable to spread the fire to the exact observed location.

Table 3: Summary of timestamps used in the simulations' verification. Locations are referred to by the name in bold font.

Approx. Coordinates of Report	Reported Local Time [MST]	Reported Location	Source	Reassigned Coordinates	Corresponding Model Output Time [MST]
(-105.174513, 39.955792)	12:18 PM	Parking lot of Costco, **Superior**	OAAR	(-105.1781, 39.9553)	12:45 PM

Approx. Coordinates of Report	**Reported Local Time [MST]**	**Reported Location**	**Source**	**Reassigned Coordinates**	**Corresponding Model Output Time [MST]**
	12:56 PM	Bill Fudale, 6th and W. Charles St., **Superior**	9News Timeline		
(-105.168723, 39.960371)	12:45 PM	**Home Depot** in Louisville (northeast side of Hwy 36)	OAAR	(-105.1716, 39.9609)	12:45 PM
(-105.194042, 39.986596)	12:46 PM	**S. Boulder** and 68th	OAAR	(-105.1933, 39.9850)	12:45 PM
(-105.166412, 39.972825)	1:33 PM	**Hillside** neighborhood, Louisville	9News Timeline	(-105.1716, 39.9736)	1:30 PM
(-105.149593, 39.954655)	4:07 PM	**Troon Ct**., Louisville	9News Timeline	(-105.1528, 39.9541)	4:00 PM
(-105.164469, 39.930960)	4:32 PM	**McC**aslin Blvd. and **Coalton** Rd.	9 News Timeline	(-105.1675, 39.9311)	4:30 PM
(-105.164465, 39.977945)	4:36 PM	South of **Harper** Lake	9News Timeline	(-105.1669, 39.9781)	4:30 PM
(-105.158023, 39.971476)	7:12 PM	**Vista Ln**. Louisville	9News Timeline	(-105.1579, 39.9721)	7:15 PM
fire perimeter	20:00 PM	Weather conditions notably changed	OAAR	fire perimeter	20:00 PM

The observation locations are used to quantify model timing and spatial agreement. Model timing is quantified through arrival times, i.e., the absolute difference between the time of observation at each of the locations and the time the simulated fire arrives at the corresponding point:

$$Arrival\ Time\ =\ t(FireArea_{\mathrm{ij}}\ >0)$$

where t is time, $FireArea_{ij}$ is the fire area at the ij grid point corresponding to an observation coordinate.

To quantify the spatial accuracy of the simulated fire area against the fire perimeter, we use a contingency table as described in (Wilks, 2011). The table summarizes the counts of combinations of possible forecast and event pairs (Figure 7). Results are analyzed in terms of the hit frequency, miss frequency, false alarm frequency, and Heidke Skill Score (HSS), also known as Cohen's Kappa.

HSS is a skill score that reflects the proportion correct that would be achieved by random forecasts that are statistically independent of the observation. HSS is 1 for perfect forecasts, forecasts equal to chance receive zero, and forecasts worse than chance receive negative scores. It is calculated as:

$$HSS\ =\ \frac{2(ad\ -\ bc)}{(a+c)(c+d)+(a+b)(b+d)}$$

where the letters a, b, c, and d correspond to the event pairs in the contingency table.

The hit frequency corresponds to the joint probability of a positive forecast and a positive outcome, the miss frequency corresponds to the joint probability of a negative forecast and a positive outcome, and the

false alarm frequency corresponds to the joint probability of a positive forecast and a negative outcome, as illustrated in Figure 7.

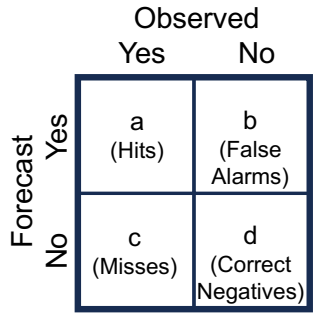

Figure 7: Counts (letters a-d) of forecast and event pairs displayed in a 2 by 2 contingency table.

4.3 Fire Forecast Results

The model experiments for the Marshall Fire illustrate the impact of firebrand spotting in fire behavior simulations. A comparison between a control simulation (CTRL) without spotting and an experiment with spot ignitions is shown in Figure 8. Panel (A) shows a comparison between CTRL and the t5n2 Fire-Spots simulation. In the CTRL experiment, the fire front is partially contained or delayed by the local road mesh, represented by a no-fuel category in the Anderson Fuels. In the t5n2 Fire-Spots experiment, the fire front spreads over the north and south sides of Marshall Rd immediately after ignition and reaches Hwy 36 within the first hour in the simulation. For a period of 9 hours from ignition time, the fire spots simulation most accurately reaches the observation locations timestamps when compared to CTRL.

Firebrand spotting can also be an important mechanism to increase the fire ROS, particularly in wind-driven fires, as noted by (Wadhwani et al., 2022) and references therein. The snapshots in Panel (B) show that spotting played a fundamental role in the rapid spread of the fire: the fire front in the t5n2 Fire-Spots experiment arrives at Hwy 36 within the first simulated hour (at 12 PM MST), whereas in the CTRL experiment, the fire front arrives 9 hours later (at 9 PM MST).

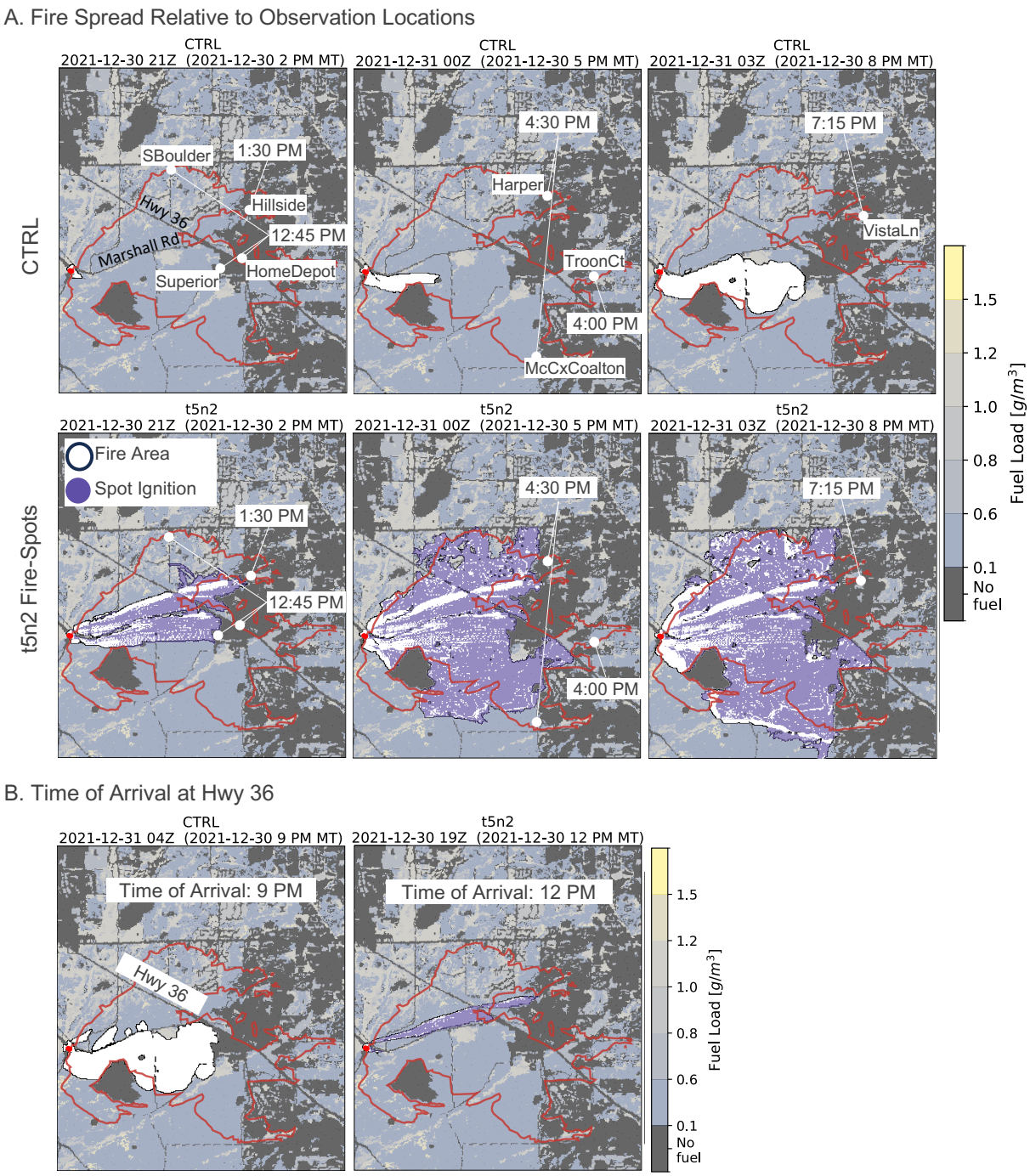

Figure 8: Numerical experiments showing CTRL and the t5n2 Fire-Spots experiment at different times into the simulation. The snapshots show the simulated fire area (white shape with black outline) and the locations of spot ignitions ahead of the fire front (purple dots). The red line indicates the fire perimeter after containment. In (A), the timestamps are compiled from video cameras where footage indicated the fire had arrived at the corresponding locations (footage sourced from 9News). The corresponding simulated time is displayed on top. In (B), the snapshots show the times the simulated fire fronts arrive at Hwy 36, with the respective times displayed on top.

The road containment clearly depicted in the CTRL simulation is simply the model's response to the fuels' characteristics in the specified fuel layer. It is known that fuel layers such as the Anderson 13-fuels (current default in WRF-Fire) and Scott and Burgan 40-fuels, are inaccurate, incomplete, and static over multiple years (DeCastro et al., 2022). The fuels in these layers are simplified representations of various vegetation types, used to parameterize Rothermel's (Rothermel, 1972) surface spread equation, and allowing for rapid application in the field, such as during suppression efforts (Price & Germino, 2022). In the region encompassed by our computational domain, the Anderson 13-fuels classifies urban fuels in a "no-fuels" category (i.e., with fuel load equal to 0 kg m^2), with the area containing the suburbs burned down by the Marshall Fire represented by short grass, hardwood litter, timber, and closed timber litter (i.e., fuel loads of 0.166, 0.78, 0.896, and 1.12 kg m^2, respectively). Even though urban structures are misrepresented by the fuel layer, it realistically represents the main local roads. The results obtained with the Fire-Spots simulations indicate that for this particular case, the lack of urban fuel representation is not the primary limitation to a more accurate simulation of fire spread. The limitation arises from the fire not being able to spot, preventing the fire front from advancing across barriers.

The forecast verification for arrival times are shown in Figure 9. Panel (A) shows the arrival times at each location in Table 3 for each of the simulations, and panel (B) displays the median times for each of the simulations, with the number of locations reached by the simulated fire indicated below the corresponding bars. The fire in CTRL reaches Superior with a 6-hour delay and it is the only location it reaches by 9 PM MT. None of the simulations is able to reach TroonCt and VistaLn, and only the simulations which favor more fire spots reach McCxCoalton (t5n1, t5n2, t3n3, t5n3, t10n1).

As expected, an increase in the thresholds for spotting results in slower fire propagation. For example, t15n3 only reaches 4 locations. In most cases, configurations with the same total threshold but with fewer neighbors propagate faster to the observation locations (e.g. t5n1 arrives faster than t5n2 at all locations). Similarly, configurations with the same number of neighbors and lower total thresholds also propagate faster (e.g. t5n2 propagates faster than t10n2). In simulations t3n5 and t5n5 the front arrives at the same time in all locations, suggesting that five neighbors is a high threshold for these simulations, such that the total threshold does not affect the results.

The simulations t10n2 and t10n3 show an opposite pattern - for the same total threshold, the higher number of neighbors actually decreases the arrival time. This is because small differences in the first hours of the simulation lead to different spotting patterns, which in turn affect the fire ROS at different locations. As shown in Figure 10, t10n2 shows a higher concentration of spot ignitions in the fire area south of Marshall Rd, whereas t10n3 shows a dense ignition area by Hwy 36 breaching the highway barrier. This is a consequence of firebrand generation being a function of fire ROS and illustrates that the outcome of these simulations is ultimately nonlinear.

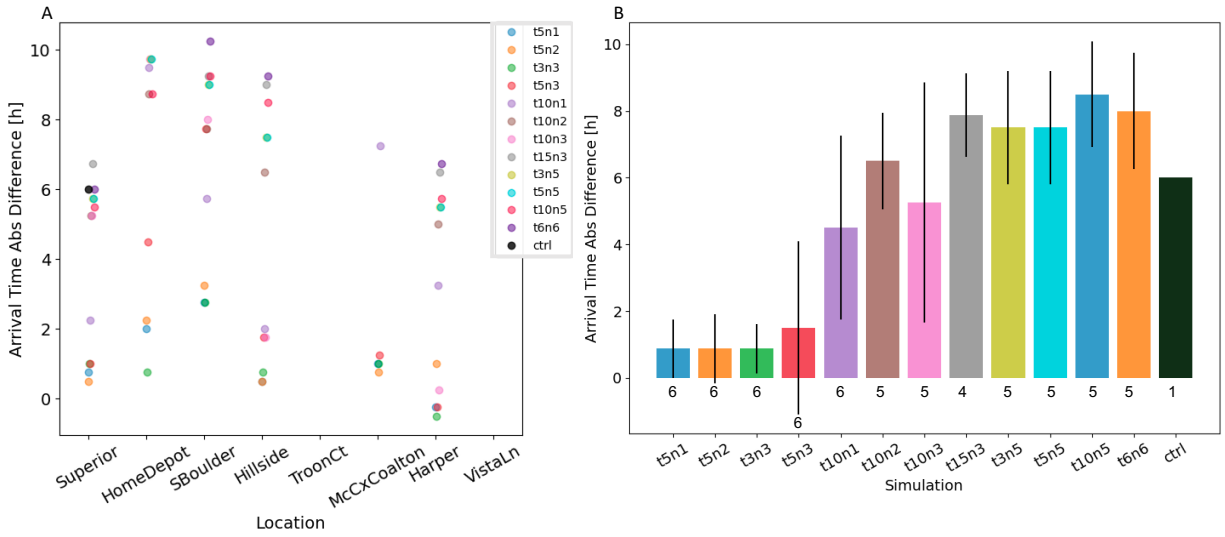

Figure 9: Arrival time of simulated fires at reported locations. (A) shows the arrival times at each location for each simulation. The circles are slightly shifted along the x-axis to facilitate visualization. (B) summarizes the results from (A) as the median times for each simulation. The number of locations reached by the fire in each of the simulations is indicated below the corresponding bars. The standard deviation is indicated by the vertical black lines.

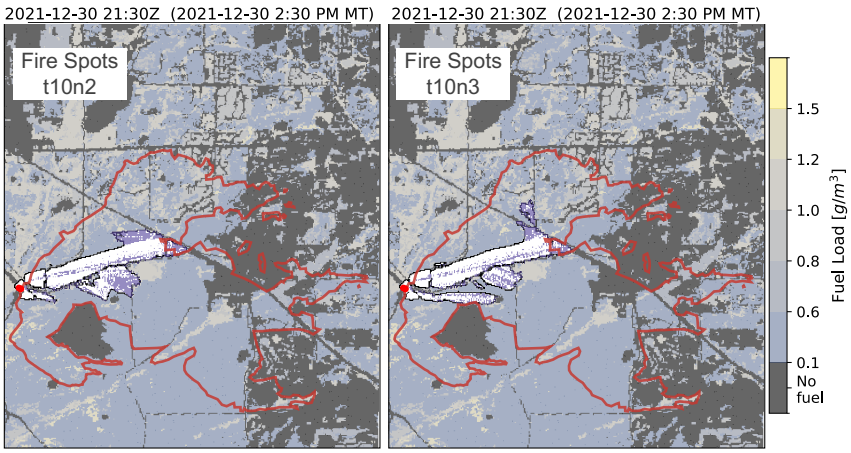

Figure 10: Nonlinear effects of firebrand generation on simulations with similar ignition criteria. The fire areas of two simulations with the same total threshold (t=10) but different neighbor thresholds (n=2 on the left and n=3 on the right) diverge due to the effect of spot ignitions on the fire rate of spread and consequent firebrand generation.

The overall spatial metrics calculated for the final fire perimeter are shown in Figure 11. Panel (A) shows the frequency of hits, misses, and false alarms between the fire perimeter and simulations at 9 PM MT. As corroborated by the point-based analysis (Figures 8 and 9), the simulations favoring more spot fires (i.e. those with fewer neighbors, and lower total threshold, e.g. t5n[1-3]) display a higher frequency of hits, indicating there was more overlap between the observed and simulated fire areas, whereas the fewer the number of spot fires (e.g. t15n3, t[3,5,10]n5, t6n6), the lower the hit frequency, with CTRL having the least

hits. Similarly, the miss frequency indicates that more of the observed perimeter was represented by the Fire-Spot simulations, with miss frequency increasing with decreasing number of spot fires. Conversely, the higher the number of spot fires, the higher the frequency of false alarms. This is because a higher number of simulated spot fires translates into a generally larger fire spread, so the tendency to overpredict is higher.

Panel (B) shows the corresponding HSS with respect to the final fire perimeter at 15-min intervals. The HSS shows that between t=0 and t=27 (4:45 PM MST), t5n1, t5n2, t3n3 are overall the most accurate predictions. This reflects the fact that the fast fire spread in these simulations produces a larger simulated fire, which is closer to the observed perimeter than the other simulations. Between t=30 (6:30 PM MST) and t=38 (8:30 PM MST), t5n3 becomes slightly more accurate, indicating that misses and false alarms in t5n1, t5n2, t3n3 are becoming more frequent as the simulated fire approaches the observed perimeter. At t=40 (9 PM MST), t10n1 yields a marginally more accurate fire spread than t5n3, whereas the skills of t5n1, t5n2, t3n3 slightly decrease (by 0.13, 0.06, and 0.09, respectively) as the simulated fire becomes larger than the observed perimeter due to a high number of fire spots. This result suggests that a mechanism to modulate of the ignition criteria could improve the overall accuracy of the parameterization and also simplify the user-defined parameter configuration.

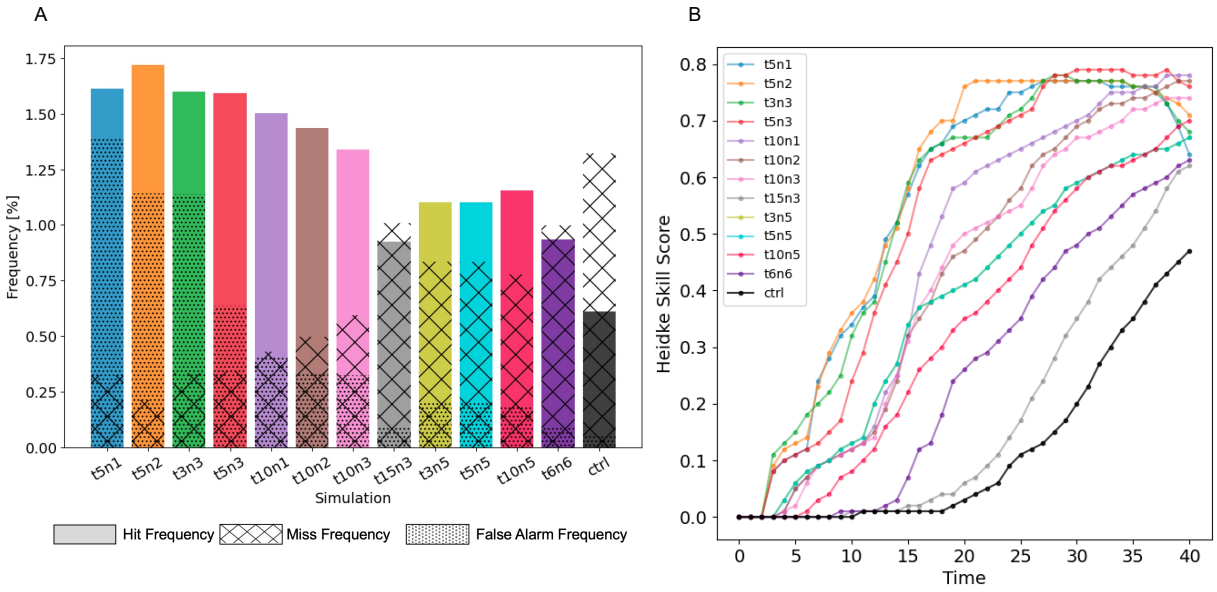

Figure 11: Spatial verification of fire spread based on fire perimeter after containment. (A) shows the hit, miss, and false alarm frequencies at 9 PM MT. (B) shows the Heidke Skill Score at 15-minute intervals.

5 Conclusions

This study describes the firebrand spotting parameterization in the WRF-Fire model. The implementation of firebrand processes for generation, transport, burnout, landing, and ignition is described alongside idealized simulations configured for coupled and uncoupled feedback between fire and atmosphere. The implemented parameterization is then applied to assess its effect on a real-case simulation of the most costly fire in the state of Colorado, the Marshall Fire, in which spot fires played a significant role in spreading the fire through an urban area.

The simulated fire is verified using a set of locations and timestamps compiled by 9News (Denver, KUSA-TV) from witnesses' recorded footage, an After-Action Review compiled by Boulder County officials, and the

official fire perimeter. We compare a control against twelve Fire-Spots simulations, and assess them in terms of arrival time and spatial metrics. All twelve Fire-Spots simulations outperform the control in all metrics. These experiments indicate spotting played a fundamental role in the rapid spread of the fire, consistent with records from the Marshall Fire and scientific literature stating that firebrands are an important mechanism to increase fire rate of spread in wind-driven fires.

These numerical experiments suggest that accounting for highly nonlinear processes, such as spot fires, can potentially improve a model ensemble and probability of outcomes, in that spotting can be a significant source of uncertainty to simulating fire spread.

Although it is known that simulated fire spread is intrinsically dependent on the model's fuels (i.e., category granularity, temporal and spatial accuracy, and resolution), when barriers such as multiple-lane highways are accurately depicted, the simulated fire cannot spread without a spotting capability. This is particularly important for research and applications utilizing model simulations where fires impact regional and local weather scales.

Our results show that the model's ability to spot can be critical for modeling fire spread over barriers present in urban and wildland areas, such as highways and bodies of water. These numerical experiments demonstrate that the underprediction of simulated fire spreads, an issue often attributed to the fire behavior parameterization and fuel data inputs, can be also caused by the presence of containment barriers, which the model is currently unable to breach. Without a spotting capability, numerical models are limited in their role to provide tactical information to operational firefighters, guide land managers, and assist researchers to better understand the various processes and the result of their interactions. In turn, this affects our collective efforts to advance wildfire science, in that the representation of mechanisms of fire spread is incomplete, impacting all stakeholders that directly or indirectly rely on information produced by numerical models.

At this stage, the firebrand spotting parameterization relies on a number of user-defined parameters to control its components. This hinders our ability to offer a more comprehensive forecast verification (e.g., multiple fires) because the results would likely depend on user configuration. The future steps envisioned for this work include the implementation of a more sophisticated generation process, transport and burnout of non-spherical particles, and modulated ignition criteria based on internal model parameters. These will certainly lead to a more robust parameterization and facilitate its configuration and use.

6 Acknowledgements

This material is based upon work supported by the National Center for Atmospheric Research, which is a major facility sponsored by the National Science Foundation under Cooperative Agreement No. 1852977. Partial funding was provided by the U.S. Army Test and Evaluation Command through an Interagency Agreement with the National Science Foundation, which sponsors NCAR. The University of Nevada, Reno team's work was supported through the National Science Foundation's Leading Engineering for America's Prosperity, Health, and Infrastructure (LEAP-HI) program by grant number CMMI1953333.

7 Data Availability Statement

The WRF-ARW model source code is available on GitHub (https://github.com/wrf-model/WRF). The firebrand spotting parameterization source code used in this study will be pushed to the WRF model repository once this manuscript is accepted for publication. It is currently hosted on a non-public repository (https://github.com/mefrediani/WRF/tree/firebrands-ignition). The Marshall Fire perimeter shapefile is available at https://www.arcgis.com/home/item.html?id=

376b3d52a6ad451ea96266aafd081b97. The Marshall Fire observation locations were compiled from https://www.marshallfiremap.com/ and are presented in Table 3.

References

. U.S. Department of Interior, Geological Survey, and U.S. Department of Agriculture. Retrieved from https://landfire.gov/fbfm13.php

. https://www.marshallfiremap.com/. Retrieved from https://www.marshallfiremap.com/

Ager, A. A., Vaillant, N. M., Finney, M. A., & others. (2011). Integrating fire behavior models and geospatial analysis for wildland fire risk assessment and fuel management planning. *Journal of Combustion*, *2011*.

Albini, F. (1983). *Potential spotting distance from wind-driven surface fires* (Research Paper No. INT-309). Odgen, UT: USDA Forest Service, Intermountain Forest and Range Experiment Station. Retrieved from https://www.fs.usda.gov/treesearch/pubs/32533

Albini, F. A. (1979). *Spot Fire Distance from Burning Trees* (General Technical Report). Missoula, MT: Intermountain Forest and Range Experiment Station.

Alexandridis, A., Russo, L., Vakalis, D., Bafas, G. V., & Siettos, C. I. (2011). Wildland fire spread modelling using cellular automata: evolution in large-scale spatially heterogeneous environments under fire suppression tactics. *International Journal of Wildland Fire*, *20*, 633–647. https://doi.org/10.1071/WF09119

Andreae, M. O., Rosenfeld, D., Artaxo, P., Costa, A. A., Frank, G. P., Longo, K. M., & Silva-Dias, M. A. F. da. (2004). Smoking rain clouds over the Amazon. *Science*, *303*(5662), 1337–1342. https://doi.org/10.1126/science.1092779

Andrews, P. L. (2018). *The Rothermel Surface Fire Spread Model and Associated Developments: A Comprehensive Explanation* (General Technical Report No. RMRS-GTR-371). Fort Collins, CO: U.S. Department of Agriculture, Forest Service, Rocky Mountain Research Station.

Andrews, P. L. (2014). Current status and future needs of the BehavePlus Fire Modeling System. *International Journal of Wildland Fire*, *23*, 21–33. https://doi.org/10.1071/WF12167

Bhutia, S., Ann Jenkins, M., & Sun, R. (2010). Comparison of firebrand propagation prediction by a plume model and a coupled–fire/atmosphere large–eddy simulator. *Journal of Advances in Modeling Earth Systems*, *2*(1).

Blaylock, B. K. (2019). *High-Resolution Rapid Refresh Model Data Analytics for Wildland Fire Weather Assessment* (PhD thesis). The University of Utah.

Bowman, D. M. J. S., Balch, J. K., Artaxo, P., Bond, W. J., Carlson, J. M., Cochrane, M. A., et al. (2009). Fire in the Earth system. *Science*, *324*(5926), 481–484. https://doi.org/10.1126/science.1163886

Coen, J. L., & others. (2013). WRF-Fire: Coupled Weather–Wildland Fire Modeling with the Weather Research and Forecasting Model. *J. Appl. Meteorol. Climatol.*, *52*, 16–38.

County, B. (2022). *Marshall Fire Operational After-Action Report* (Operational After-Action Report). Boulder County Office of Emergency Management.

DeCastro, A., Siems-Anderson, A., Smith, E., Knievel, J. C., Kosović, B., Brown, B. G., & Balch, J. K. (2022). Weather Research and Forecasting—Fire Simulated Burned Area and Propagation Direction Sensitivity to Initiation Point Location and Time. *Fire*, *5*(3), 58.

DeCastro, A. L., Juliano, T. W., Kosović, B., Ebrahimian, H., & Balch, J. K. (2022). A computationally efficient method for updating fuel inputs for wildfire behavior models using Sentinel imagery and random forest classification. *Remote Sensing*, *14*(6), 1447.

Dougherty, M. T., & Johnson, C. (2023). *Marshall Fire Investigative Summary*. Boulder County. Retrieved from https://assets.bouldercounty.gov/wp-content/uploads/2023/06/marshall-fire-investigative-summary.pdf

Dowell, D. C., Alexander, C. R., James, E. P., Weygandt, S. S., Benjamin, S. G., Manikin, G. S., et al. (2022). The High-Resolution Rapid Refresh (HRRR): An Hourly Updating Convection-Allowing Forecast Model. Part I: Motivation and System Description. *Weather and Forecasting*, *37*(8). https://doi.org/10.1175/waf-d-21-0151.1

Dudhia, J. (1989). Numerical study of convection observed during the Winter Monsoon Experiment using a mesoscale two-dimensional model. *Journal of the Atmospheric Sciences*, *46*(20), 3077–3107.

Ek, M. B., Mitchell, K. E., Lin, Y., Rogers, E., Grunmann, P., Koren, V., et al. (2003). Implementation of Noah land surface model advances in the National Centers for Environmental Prediction operational mesoscale Eta model. *Journal of Geophysical Research: Atmospheres*, *108*(D22).

Ellis, P. F. (2015). The likelihood of ignition of dry-eucalypt forest litter by firebrands. *Int. J. Wildland Fire*, *24*(2), 225–235.

Ervilha, A. R., Pereira, J. M. C., & Pereira, J. C. F. (2017). On the parametric uncertainty quantification of the Rothermel's rate of spread model. *Applied Mathematical Modelling*, *41*, 37–53. https://doi.org/10.1016/j.apm.2016.06.026

Fernandez-Pello, A. C. (2017). Wildland fire spot ignition by sparks and firebrands. *Fire Safety Journal*, *91*, 2–10. https://doi.org/10.1016/j.firesaf.2017.04.040

Filippi, J.-B., Morandini, F., Balbi, J. H., & Hill, D. R. (2010). Discrete event front-tracking simulation of a physical fire-spread model. *Simulation*, *86*(10), 629–646.

Filkov, A., Prohanov, S., Mueller, E., Kasymov, D., Martynov, P., Houssami, M. E., et al. (2017). Investigation of firebrand production during prescribed fires conducted in a pine forest. *Proceedings of the Combustion Institute*, *36*(2), 3263–3270. https://doi.org/10.1016/j.proci.2016.06.125

Finney, M. A. (1998). *FARSITE, Fire Area Simulator–model development and evaluation*. US Department of Agriculture, Forest Service, Rocky Mountain Research Station.

Finney, M. A. FlamMap: Fire Behavior Mapping and Analysis Program. Retrieved from https://www.firelab.org/project/flammap

Fovell, R. G., Brewer, M. J., & Garmong, R. J. (2022). The December 2021 Marshall Fire: Predictability and Gust Forecasts from Operational Models. *Atmosphere*, *13*, 765.

Frediani, M., Juliano, T. W., DeCastro, A., Kosovic, B., & Knievel, J. (2022). A Fire-Spotting Parameterization Coupled with the WRF-Fire Model. *Authorea Preprints*.

Frediani, M., Juliano, T. W., Knievel, J. C., Tessendorf, S. A., & Kosovic, B. (2022). The role of fire spotting in fire-weather prediction. *Authorea Preprints*. https://doi.org/10.1002/essoar.10512599.1

Frediani, M. E., Juliano, T. W., Knievel, J. C., Kosovic, B., & Tessendorf, S. A. (2023). The Role of Fire Spotting in Fire-Weather Prediction. In *Proceedings of the 103rd American Meteorological Society Annual Meeting*. Denver, CO. Retrieved from https://ams.confex.com/ams/103ANNUAL/meetingapp.cgi/Session/63279

Frediani, M. E. B., & Rodriguez, C. A. M. (2008). Description of the cloud hydrometeors observed in the Amazon region during the wet and dry season. *Meteorologica*, *33*, 1–10.

Freire, J. G., & DaCamara, C. C. (2019). Using cellular automata to simulate wildfire propagation and to assist in fire management. *Natural Hazards and Earth System Sciences*, *19*, 169–179. https://doi.org/10.5194/nhess-19-169-2019

Haupt, S. E., Kosovic, B., Shaw, W., Berg, L. K., Churchfield, M., Cline, J., et al. (2019). On bridging a modeling scale gap: Mesoscale to microscale coupling for wind energy. *Bulletin of the American Meteorological Society*, *100*(12), 2533–2550.

Himoto, K., & Iwami, T. (2021). Generalization framework for varying characteristics of the firebrand generation and transport from structural fire source. *Fire Safety Journal*, *125*, 103418.

Hong, S.-Y., Dudhia, J., & Chen, S.-H. (2006). A revised approach to ice microphysical processes for the bulk parameterization of clouds and precipitation. *Monthly Weather Review*, *132*(1), 103–120.

Hong, S.-Y., & Lim, J. (2006). A new vertical diffusion package with an explicit treatment of entrainment processes. *Monthly Weather Review*, *134*(9), 2318–2341.

Iacono, M. J., Delamere, J. S., Mlawer, E. J., Shephard, M. W., Clough, S. A., & Collins, W. D. (2008). Radiative forcing by long-lived greenhouse gases: Calculations with the AER radiative transfer models. *Journal of Geophysical Research: Atmospheres*, *113*.

Jiménez, P. A., Dudhia, J., González-Rouco, J. F., Navarro, J., Montávez, J. P., & García-Bustamante, E. (2012). A Revised Scheme for the WRF Surface Layer Formulation. *Monthly Weather Review*, *140*(3). https://doi.org/10.1175/mwr-d-11-00056.1

Jolliffe, I. T., & Stephenson, D. B. (2012). *Forecast verification: a practitioner's guide in atmospheric science*. John Wiley & Sons.

Juliano, T. W., Lareau, N., Frediani, M. E., Shamsaei, K., Eghdami, M., Kosiba, K., et al. (2023). Toward a Better Understanding of Wildfire Behavior in the Wildland-Urban Interface: A Case Study of the 2021 Marshall Fire. *Geophysical Research Letters*, *50*(10), e2022GL101557.

Koo, E., Pagni, P. J., & Linn, R. R. (2007). Using FIRETEC to describe firebrand behavior in wildfires. In *10th International Conference on Fire and Materials 2007*.

Lee, C.-Y., & Chen, S. S. (2014). Stable boundary layer and its impact on tropical cyclone structure in a coupled atmosphere–ocean model. *Monthly Weather Review*, *142*(5), 1927–1944.

Linn, R., Reisner, J., Colman, J. J., & Winterkamp, J. (2002). Studying wildfire behavior using FIRETEC. *International Journal of Wildland Fire*, *11*(4), 233. https://doi.org/10.1071/wf02007

Linn, R. R., Goodrick, S. L., Brambilla, S., Brown, M. J., Middleton, R. S., O'Brien, J. J., & Hiers, J. K. (2020). QUIC-fire: A fast-running simulation tool for prescribed fire planning. *Environmental Modelling and Software*, *125*, 104616. https://doi.org/10.1016/j.envsoft.2019.104616

Mandel, J., Amram, S., Beezley, J. D., Kelman, G., Kochanski, A. K., Kondratenko, V. Y., et al. (2014). Recent advances and applications of WRF–SFIRE. *Natural Hazards and Earth System Sciences*, *14*(10), 2829–2845.

Manzello, S. L., Suzuki, S., Gollner, M. J., & Fernandez-Pello, A. C. (2020). Role of firebrand combustion in large outdoor fire spread. *Progress in Energy and Combustion Science*, *76*, 100801. https://doi.org/10.1016/j.pecs.2019.100801

Masoudvaziri, N., Bardales, F. S., Keskin, O. K., Sarreshtehdari, A., Sun, K., & Elhami-Khorasani, N. (2021). Streamlined wildland-urban interface fire tracing (SWUIFT): modeling wildfire spread in communities. *Environmental Modelling & Software*, *143*, 105097.

McArthur, A. G. (1967). *Fire Behaviour in Eucalypt Forests*. Canberra, Australia: Department of National Development, Commonwealth of Australia.

McArthur, A. G. (1967). Fire behaviour in Eucalypt forests. (p. 35).

McGinnis, S., Kessenich, L., Mearns, L., Cullen, A., Podschwit, H., & Bukovsky, M. (2023). Future regional increases in simultaneous large Western USA wildfires. *International Journal of Wildland Fire*, *32*, 1304–1314. https://doi.org/10.1071/WF22107

Mell, W., Jenkins, M. A., Gould, J., & Cheney, P. (2007). A physics-based approach to modelling grassland fires. *International Journal of Wildland Fire*, *16*(1), 1. https://doi.org/10.1071/wf06002

Mell, W., Simeoni, A., Morvan, D., Hiers, J. K., Skowronski, N., & Hadden, R. M. (2018). Clarifying the meaning of mantras in wildland fire behaviour modelling: reply to Cruz et al. (2017). *International Journal of Wildland Fire*, *27*, 770–775. https://doi.org/10.1071/WF18106

Murphy, A. H. (1996). The Finley affair: A signal event in the history of forecast verification. *Weather and Forecasting*, *11*(1), 3–20.

Murphy, A. H., & Winkler, R. L. (1987). A general framework for forecast verification. *Monthly Weather Review*, *115*(7), 1330–1338.

Price, S. "jake", & Germino, M. J. (2022). Simulation of a historic megafire in sagebrush steppe using FARSITE: inaccuracies resulting from LANDFIRE inputs rectified using readily available vegetation maps derived from satellite imagery. Retrieved from https://doi.org/10.21203/rs.3.rs-1047854/v1

Roberts, M., Lareau, N., Juliano, T. W., Shamsaei, K., Ebrahimian, H., & Kosovic, B. (2023). Sensitivity of Simulated Fire-Generated Circulations to Fuel Characteristics During Large Wildfires. *Authorea Preprints*. https://doi.org/10.22541/essoar.169264796.69205142

Rothermel, R. C. (1972). *A mathematical model for predicting fire spread in wildland fuels* (Vol. 115). Intermountain Forest & Range Experiment Station, Forest Service, US ....

Sanjuan, G., Brun, C., Margalef, T., & Cortés, A. (2014). Wind field uncertainty in forest fire propagation prediction. *Procedia Computer Science*, *29*, 1535–1545. https://doi.org/10.1016/j.procs.2014.05.139

Skamarock, W. C., Klemp, J. B., Dudhia, J., Gill, D. O., Liu, Z., Berner, J., et al. (2021). *A Description of the Advanced Research WRF Model Version 4.3* (Technical Note No. NCAR/TN-556+STR). National Center for Atmospheric Research. https://doi.org/10.5065/1dfh-6p97

Stein, A. F., Draxler, R. R., Rolph, G. D., Stunder, B. J. B., Cohen, M. D., & Ngan, F. (2015). SUPPLEMENT: DETAILED DESCRIPTION OF THE MODEL UPDATES. *Bulletin of the American Meteorological Society*, *96*(12), ES203–ES207.

Storey, M. A., & others. (2021). Experiments on the influence of spot fire and topography interaction on fire rate of spread. *PLoS One*, *16*, e0245132.

Tarifa, C. S. (1967). *Transport and Combustion of Firebrands* (Vol. 2). Madrid, Spain: Instituto Nacional de Tecnica Aeroespacial, Esteban Terradas.

Tarifa, C. S., Notario, P. P. del, & Moreno, F. G. (1965). On the flight paths and lifetimes of burning particles of wood. *Proceedings of the Combustion Institute*, *10*, 1021–1037.

Tohidi, A., Kaye, N., & Bridges, W. (2015). Statistical description of firebrand size and shape distribution from coniferous trees for use in Metropolis Monte Carlo simulations of firebrand flight distance. *Fire Safety Journal*, *77*. https://doi.org/10.1016/j.firesaf.2015.07.008

Tohidi, A., & Kaye, N. B. (2017). Stochastic modeling of firebrand shower scenarios. *Fire Safety Journal*, *91*, 91–102.

Tse, S. D., & Fernandez-Pello, A. C. (1998). On the flight paths of metal particles and embers generated by power lines in high winds–a potential source of wildland fires. *Fire Safety Journal*, *30*(4), 333–356.

Tymstra, C., Bryce, R. W., Wotton, B. M., Taylor, S. W., Armitage, O. B., & others. (2010). Development and structure of Prometheus: the Canadian wildland fire growth simulation model. *Natural Resources*

Canada, Canadian Forest Service, Northern Forestry Centre, Information Report NOR-X-417.(Edmonton, AB).

Wadhwani, R., Sullivan, C., Wickramasinghe, A., Kyng, M., Khan, N., & Moinuddin, K. (2022). A review of firebrand studies on generation and transport. *Fire Safety Journal*, 103674.

Wilks, D. S. (2011). *Statistical methods in the atmospheric sciences* (Vol. 100). Academic press.

Witty, W. H. (1964). A new method of numerical integration of differential equations. *Mathematics of Computation*, *18*(87), 497–500.

Woycheese, J. P., Pagni, P. J., & Liepmann, D. (1998). *Brand Lofting above Large-Scale Fires.* Building and Fire Research Laboratory, National Institute of Standards and Technology.

Xue, H., Hu, X., Dahl, N., & Xue, M. (2012). Post-frontal combustion heat modeling in DEVS-FIRE for coupled atmosphere-fire simulation. *Procedia Comput. Sci.*, *9*, 302–311.

Computational and Information Systems Laboratory, CISL. (2023). *Derecho: HPE Cray EX System (NCAR Community Computing).* Boulder, CO: National Center for Atmospheric Research (NCAR).